

Interrogation of 2,2'-Bipyrimidines as Low-Potential Two-Electron Electrolytes

Jeremy D. Griffin, Adam R. Pancoast, and Matthew S. Sigman*



Cite This: *J. Am. Chem. Soc.* 2021, 143, 992–1004



Read Online

ACCESS |



Metrics & More

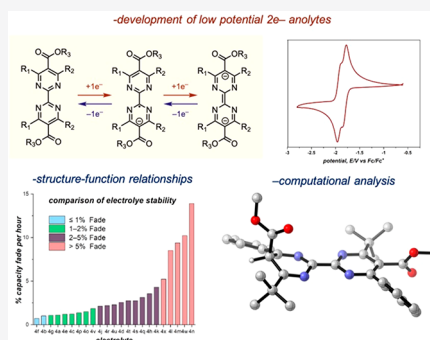


Article Recommendations



Supporting Information

ABSTRACT: As utilization of renewable energy sources continues to expand, the need for new grid energy storage technologies such as redox flow batteries (RFBs) will be vital. Ultimately, the energy density of a RFB will be dependent on the redox potentials of the respective electrolytes, their solubility, and the number of electrons stored per molecule. With prior literature reports demonstrating the propensity of nitrogen-containing heterocycles to undergo multielectron reduction at low potentials, we focused on the development of a novel electrolyte scaffold based upon a 2,2'-bipyrimidine skeleton. This scaffold is capable of storing two electrons per molecule while also exhibiting a low (~ -2.0 V vs Fc/Fc⁺) reduction potential. A library of 24 potential bipyrimidine anolytes were synthesized and systematically evaluated to unveil structure–function relationships through computational evaluation. Through analysis of these relationships, it was unveiled that steric interactions disrupting the planarity of the system in the reduced state could be responsible for higher levels of degradation in certain anolytes. The major decomposition pathway was ultimately determined to be protonation of the dianion by solvent, which could be reversed by electrochemical or chemical oxidation. To validate the hypothesis of strain-induced decomposition, two new electrolytes with minimal steric encumbrance were synthesized, evaluated, and found to indeed exhibit higher stability than their sterically hindered counterparts.



INTRODUCTION

Renewable energy sources are expected to play an increasingly important role in the global energy supply.^{1–3} However, common renewable energy technologies, such as solar or wind power, suffer from intermittent energy generation that could cause grid stability issues.^{4–6} To overcome this limitation, large scale energy storage systems need to be developed, including redox flow batteries (RFBs).^{7–9} These systems store electrical energy by flowing redox-active compounds (electrolytes) on opposite sides of an electrochemical cell, simultaneously reducing anolytes and oxidizing catholytes in the course of charging. During discharge of the battery, the opposite redox event is performed. RFBs have traditionally been dominated by the use of aqueous vanadium systems due to their long lifetimes and efficient cycling capabilities.^{10,11} However, from environmental, sustainability, and economic perspectives, these systems are not ideal.^{12–15}

Organic electrolytes can hypothetically reach higher cell voltages (and thus energy densities) because they are soluble in nonaqueous and aqueous conditions,¹⁶ while simultaneously addressing environmental and sustainability concerns. Nonaqueous solvents such as acetonitrile (MeCN) offer a much larger potential window (~ 6 V) than that of H₂O (1.23 V)¹⁷ and are capable of solubilizing organic electrolytes as well as supporting electrolyte salts. While significant progress has been reported,^{18,19} organic electrolytes with redox potentials at the bounds of the electrochemical window of MeCN have not yet

been developed. This could be in part due to the inherently more reactive (from a thermodynamic perspective) nature of electrolytes with extreme redox potentials. Specifically, redox events at extreme potentials will produce low-lying unfilled molecular orbitals (MOs) for catholytes or high-lying occupied MOs for anolytes. Therefore, accomplishing the goal of maximizing the voltage of nonaqueous RFBs will require more systematic studies into the fundamental properties of organic electrolytes that have both high chemical stability and extreme redox potentials. Additionally, the energy density of RFBs can be improved through the development of electrolytes that can access multiple charged states; this has been accomplished in transition metal-based electrolytes^{20,21} but has proven more difficult in organic systems.^{22–24} Commonly used anolytes such as 9-fluorenone²⁵ and alkylated phthalimide derivatives^{18,26} are limited to the storage of a single electron in the charged state. Other systems, including viologen derivatives,²² 4-benzoylpyridiniums,²⁷ and anthraquinone derivatives,^{23,28} have been shown to undergo two reductions,

Received: October 26, 2020

Published: January 7, 2021



however, one or both of the reduction potentials occurs at relatively moderate potentials (Figure 1).

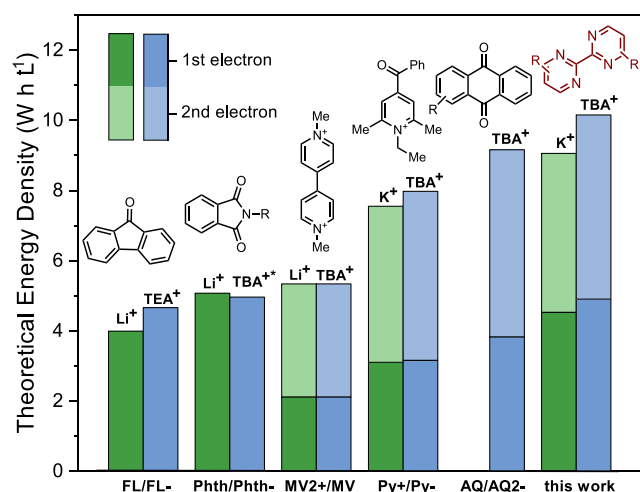


Figure 1. Comparison of the theoretical energy density of various anolyte materials (half-cell) with 0.1 M active electrolyte. Green and blue bars show the energy densities when using coordinating (green) and noncoordinating (blue) supporting electrolytes. FL = 9-fluorenone, Phth = *N*-alkyl phthalimide, MV = methyl viologen, Py = 4-benzoylpyridinium, AQ = anthraquinone.

With this context in mind, our goal was to identify and study electrolytes that could probe how one can simultaneously optimize both the number of electrons stored per small molecule and extreme redox potentials. To achieve this goal, herein we present a combined experimental and computational study of a new class of $2e^-$, low-potential anolytes derived from a bipyrimidine core. A modular synthetic route was developed that enabled the synthesis of a library of analogues, which were evaluated for stability during electrochemical cycling. Structure–function relationships using a computational workflow provided insights into what is required to achieve enhanced cycling stability.

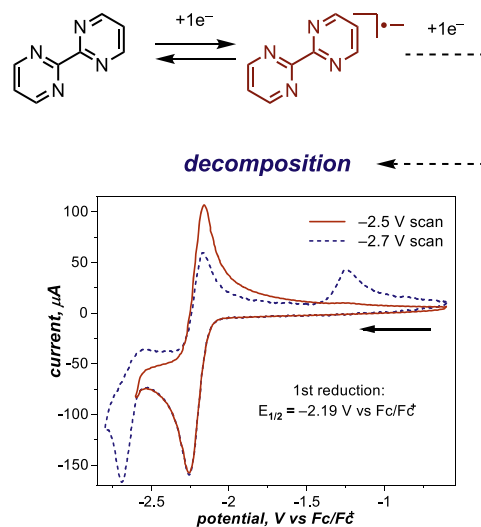
RESULTS AND DISCUSSION

Electrolyte Scaffold Selection and Synthesis. In 2015, Sanford and co-workers disclosed the development of pyridinium-based anolytes, which have subsequently been studied to improve their stability and energy density by employing both classical and modern physical organic tools.^{29,30} Preliminary investigations by our team, as well as previous reports from the Sanford lab,²⁹ revealed that other nitrogen-based heterocycles were capable of undergoing reversible reduction at low potentials near the solvent window (approaching -2.0 V vs Fc/Fc⁺). Of particular interest were bis-heterocycles, such as bipyridines, as these molecules are commonly employed in metal complexes as nonredox innocent ligands.^{31–33} Additionally, these molecules present the possibility of undergoing two consecutive reductions (in a manner akin to viologen)^{22,34–36} at lower potentials. While several substituted (particularly 5,5'-substituted) bipyridines were found to have two reversible redox couples at low potentials, ultimately bipyridines were not conducive to systematic analysis, in part, due to the lack of a modular route to their synthesis.

As a result, other nitrogen heterocycle-containing molecules, which could be more amenable to derivatization, were

investigated. Initial evaluation of several bis-heterocycle core structures revealed that unsubstituted 2,2'-bipyrimidine was a particularly promising redox-active subunit, which exhibited a single reversible couple within the solvent window, at low potential ($E_{1/2}^{\text{red}} = -2.19$ V vs Fc/Fc⁺). While a second redox event was observed ($E_{p/2}^{\text{red}} = \sim -2.6$ V), this couple was irreversible and accessing it led to obvious decomposition on the CV time scale (Figure 2A). It was hypothesized that

A: examining bis-heterocycles as potential $2e^-$ anolytes



B: design of 2nd generation $2e^-$ electron anolytes

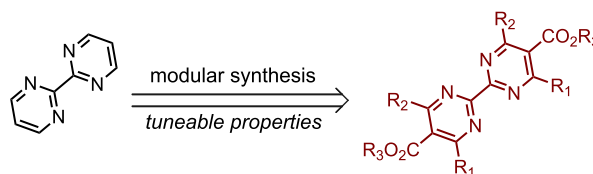


Figure 2. (A) Cyclic voltammograms of 2,2'-bipyrimidine (5 mM) in 0.1 M TBABF₄/MeCN solution with switching potential at -2.6 and -2.8 V, respectively. Glassy carbon working electrode (0.07 cm²). Scan rate = 100 mV/s. (B) Designing a new anolyte that can store $2e^-$ at extreme redox potentials.

addition of electron-withdrawing groups onto the bipyrimidine core could shift the second redox potential into the solvent window; consequently, a synthetic route was designed to access more electron-deficient ester-substituted bipyrimidines (Figure 2B). The route was inspired by Buono and co-workers in their synthesis of hydroxypyrimidines,³⁷ which have been demonstrated as important intermediates for the synthesis of pharmaceuticals. An exciting aspect of the synthetic plan was the use of a Biginelli condensation, which would theoretically allow us to vary substitution at all three of the available positions on the pyrimidine core due to the availability of a wide variety of both aldehyde and ketoester starting materials.

This synthetic strategy afforded the opportunity to design a subset of these molecules to study structure–function relationships (vide infra). Typical Biginelli conditions (Figure 3, condition i) involved CuCl and H₂SO₄ in catalytic quantities; however, in the case of aliphatic aldehydes, FeCl₃·6H₂O was used as a superior alternative (condition ii).³⁸ The pyrimidinone products (1) following condensation can be

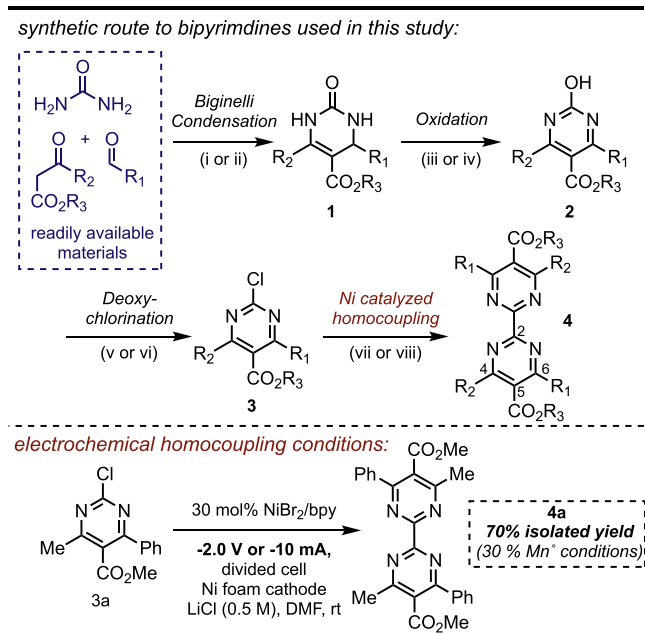


Figure 3. Synthetic route to substituted 2,2'-bipyrimidines: (i) 1 mol % CuCl₂, 20 mol % H₂SO₄, R₃OH, 70 °C; (ii) 0.6 equiv of FeCl₃·6H₂O, HCl, R₃OH Δ; (iii) 1 mol % CuCl₂, 20 mol % K₂CO₃, 2.0 equiv of *t*BuOOH, DCM, 40 °C; (iv) 1.2 equiv of K₂S₂O₈, 3:2 MeCN:H₂O, Δ; (v) 0.5 equiv of *N,N*-dimethylaniline, 8.5 equiv of POCl₃, 60–70 °C; (vi) 5.0 equiv of PPh₃, 5.0 equiv of *N*-chlorosuccinimide, dioxane, Δ; (vii) 5–10 mol % NiBr₂, 10 mol % 2,2'-bipyridine, 2.0 equiv of Mn⁺, DMF 60 °C; (viii) electrochemical conditions, see above.

efficiently converted to the corresponding 2-hydroxypyrimidines (**2**) via oxidation. In most cases, oxidation could be achieved under the catalytic CuCl₂ conditions described by Buono and co-workers utilizing *t*BuOOH as a mild stoichiometric oxidant (condition iii).³⁷ In the case of ortho-substituted aromatic groups (R₁ = 2-aryl), oxidation proceeded slowly under these conditions. Thus, oxidation of these substrates could be achieved more efficiently using stoichiometric K₂S₂O₈ (condition iv). Importantly, the first two steps in the sequence have been reported to be highly scalable (~400 kg scale, conditions i and iii)³⁷ without the need for purification (products **1** and **2** could be obtained cleanly through a simple filtration in most cases).

Converting 2-hydroxypyrimidines (**2**) to their respective 2-chloropyrimidines (**3**) proceeded smoothly through the use of POCl₃ (condition v),³⁹ with the exception of acid-sensitive esters which required the use of Appel type conditions (condition vi).^{40,41} Finally, a Ni-catalyzed homocoupling, originally developed for the synthesis of bipyridines by Weix and co-workers, could be adapted to the synthesis of the desired bipyrimidine products (**4**).⁴² While these conditions were not optimized for a particular substrate, it was discovered that some minor changes could furnish the products with higher efficiency (see SI for details). Additionally, the reductive homocoupling can be carried out electrochemically to provide **4a** in much higher yield relative to the Mn-mediated conditions (Figure 3, see SI for details).⁴³

Characterization of a Model Electrolyte. Cyclic voltammetry (CV) experiments with compound **4a** showed that these substituted bipyrimidines undergo two reversible redox events (Figure 4), initially confirmed via coulometry.

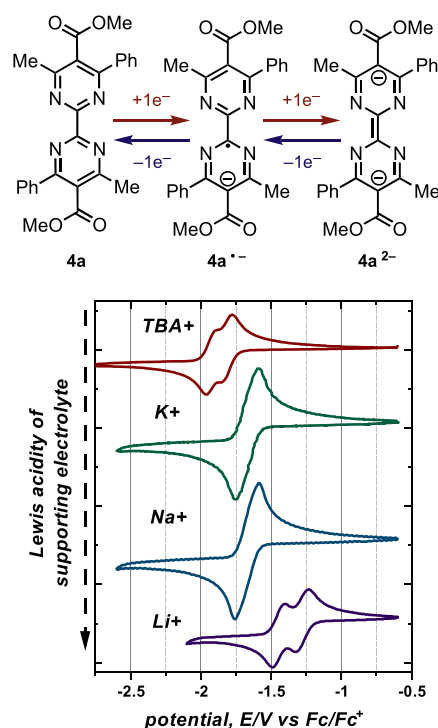
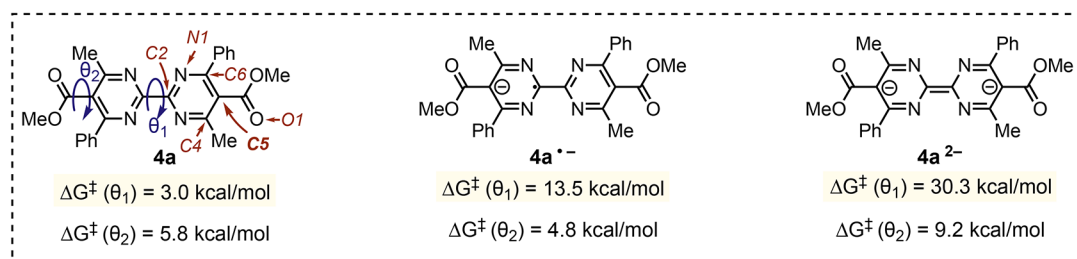


Figure 4. Cyclic voltammograms of compound **4a** with TBAPF₆, KPF₆, NaPF₆, and LiPF₆ (0.5 M) as supporting electrolytes in MeCN. Glassy carbon working electrode (0.07 cm²). Scan rate = 100 mV/s scan rate.

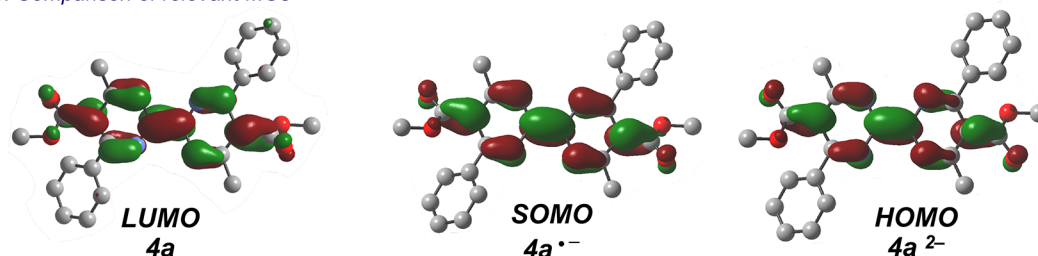
Two-electron electrolytes can suffer loss of energy efficiency if the redox couples of the individual electron transfers are very different. If redox couples are sufficiently separated, a significant amount of energy can be lost in the form of heat.²⁷

Surprisingly, 2,2'-bipyrimidines containing esters at the 5,5' positions were found to undergo two successive reduction events at similar potentials (−1.83 and −2.00 V vs Fc/Fc⁺, respectively); in some cases, the redox potential for both couples are nearly identical (vide infra). The nature of the two redox events is dependent, in part, on the identity of the counterions associated with the reduced state (Figure 4). More Lewis acidic counter cations lead to an anodic shift in potential, a phenomenon also observed for the second reduction of pyridinium-based electrolytes.²⁷ This is rationalized by the stronger coordination of the counteranion with the anionic products of reduction. Interestingly, the use of KPF₆ or NaPF₆ as the supporting electrolyte not only causes a shift in redox potential of **4a** (relative to TBAPF₆) but also causes both reduction waves to coalesce into a single discernible, albeit broad (i.e., peak-to-peak separation ≠ 28.5 mV) redox event. This indicates that the two couples are shifted closer together but still thermodynamically inequivalent. LiPF₆ resulted in the most dramatic shift in *E*_{1/2}; however, both redox events were again resolved into two distinct peaks. While it is not clear why the relative difference in the two redox couples are affected by the cation identity, it is possible this arises from differences in how each counteranion interacts with the anion and dianion reduction products, respectively.⁴⁴

To better understand the nature of both reduction products, DFT calculations were undertaken. Using **4a** as a model system, geometry optimizations were carried out on the neutral (**4a**), radical-anion (**4a**^{•−}), and dianion (**4a**^{2−}) charge states at the M06-2X/6-31+G(d,p) level of theory⁴⁵ with the

A: Computed rotational barriers (θ_1 and θ_2) for $4a$, $4a^{\bullet-}$, and $4a^{2-}$ 

B: Comparison of relevant MOs



C: Charge and spin density change after each reduction

Atom Label	Δ NBO Charge ($4a \rightarrow 4a^{\bullet-}$)	Δ NBO Charge ($4a^{\bullet-} \rightarrow 4a^{2-}$)	Spin density ($4a^{\bullet-}$)
C2	-0.100	-0.096	0.191
C5	-0.124	-0.111	0.225
O1	-0.045	-0.073	0.038
N1	-0.045	-0.032	0.067

Figure 5. (A) Rotational barriers of $4a$, $4a^{\bullet-}$, and $4a^{2-}$ were computed by scanning θ_1 and θ_2 in 5° increments to find the highest energy structure, which was used as the input geometry for transition state calculations. θ_1 dihedral angle between the two pyrimidine rings. θ_2 is the dihedral angle between the ester and the pyrimidine ring (smallest angle). (B) Relevant molecular orbitals of $4a$, $4a^{\bullet-}$, and $4a^{2-}$. (C) Changes in NBO charge at relevant atoms upon reduction from $4a \rightarrow 4a^{\bullet-}$ and $4a^{\bullet-} \rightarrow 4a^{2-}$. Mulliken spin density from $4a^{\bullet-}$. All calculations were performed at the M06-2X/6-31+G(d,p) level of theory with CPCM solvation in MeCN.

conductor-like polarizable continuum model (CPCM)^{46,47} solvation in acetonitrile. In the optimized geometry of $4a$, the two heterocycles do not adopt a planar conformation, although the barrier to rotation around the bond is predicted to be low ($\Delta\Delta G^\ddagger_{\theta_1} = \sim 3$ kcal/mol, Figure 5A).⁴⁸ The LUMO has symmetry similar to that of the SOMO of $4a^{\bullet-}$, suggesting a relatively small geometrical change following reduction (Figure 5B). Because the barrier to rotation is low, adopting the conformation necessary for the electron transfer to occur should be facile. $4a^{\bullet-}$ takes on a planar geometry, with respect to the two heterocycles, with the barrier to rotation increasing to 13.5 kcal/mol, demonstrating the increase in bond order. Due to this relatively low barrier for rotation, in cases where substituents on the heterocycle are not identical, an equilibrium mixture of both conformers will likely be formed following electron transfer. The HOMO of $4a^{2-}$ demonstrates symmetry similar to that of the SOMO of $4a^{\bullet-}$, while the bond order between the central heterocycles increases further as demonstrated by an even higher barrier to rotation (30.3 kcal/mol). This large barrier indicates that isomerization is not likely occurring at room temperature in the dianionic state; thus, the isomeric mixture obtained is likely dictated by the distribution of $4a^{\bullet-}$.

As a result of steric repulsion with the substituents at the 4 and 6 positions, the ester does not achieve coplanarity with the pyrimidine ($4a$, $\theta_2 = 55^\circ$). The dihedral angle between each of the heterocycles and the connected ester functionalities is reduced in each subsequent electron transfer event, demonstrating the importance of delocalization of the charge onto the

ester. After the first reduction, $\Delta G^\ddagger_{(\theta_2)}$ decreases because coplanarity allows delocalization of the anionic charge (Figure 5A). In $4a^{2-}$, a coplanar conformation is adopted, however the barrier to rotation remains accessible at room temperature ($\Delta G^\ddagger_{(\theta_2)} = 9.2$ kcal/mol). This implies a relatively small bond order between the two groups, and that the anionic charge primarily resides at the C5 position. The equilibrium distribution between the ester conformers is likely controlled by steric interactions of the ester with substituents at the 4 and 6 positions of the ring. The presence of multiple conformers/isomers could have interesting implications for redox properties and solubility of the reduced species.

NBO calculations reveal that the largest increase of negative charge is at the C2 and C5 carbons for $4a \rightarrow 4a^{\bullet-}$ and $4a^{\bullet-} \rightarrow 4a^{2-}$, although there is significant increase in negative charge at the heteroatoms as well (Figure 5C). Further, natural population analysis also suggests a formal lone pair on the C5 carbon with an occupancy of 1.32 electrons for $4a^{2-}$. MO analysis shows that in the SOMO and HOMO of $4a^{\bullet-}$ and $4a^{2-}$, respectively, a relatively localized lobe at the C5 position is present (Figure 5B). Similarly, the spin density in $4a^{\bullet-}$ seems to be primarily localized at the C2 and C5 positions as predicted by Mulliken population analysis. Thus, while the ester group has an effect of stabilizing anionic charge in the reduced states, a formal anionic charge is not observed on the carbonyl oxygen as intuitively anticipated, but rather, due to the distortion of the ester from planarity, lies more so on the C5 positions. This result informed our later analysis of how the reduced electrolytes decompose (vide infra).

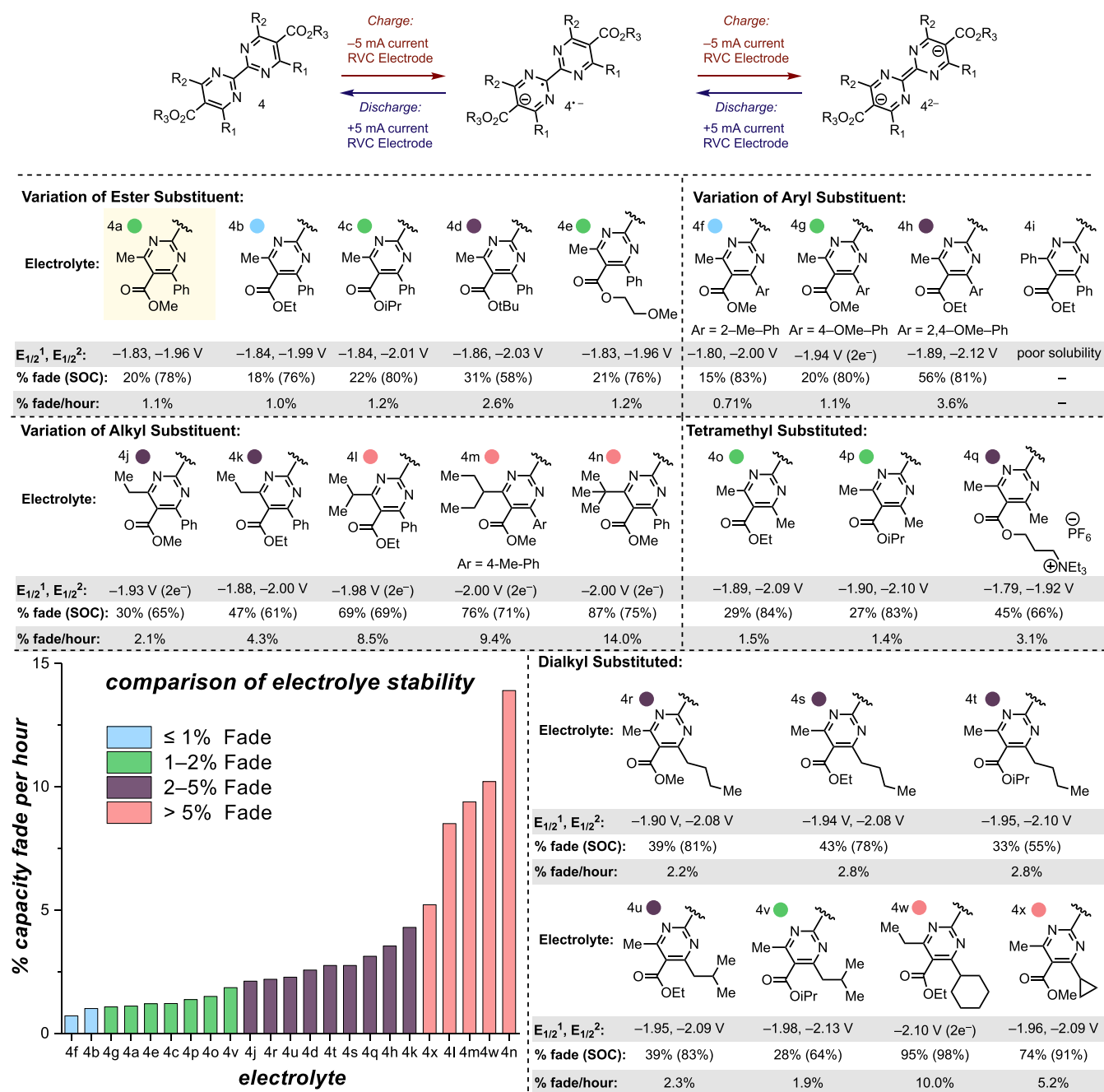


Figure 6. Library of 2,2'-bipyrimidines. Redox potentials referenced internally vs Fc/Fc⁺. %Fade = the overall capacity fade observed for each compound. SOC = state of charge (highest reached). % Fade/h = overall capacity fade/total cycling time.

Evaluation of the Electrolyte Library for Cycling Stability. After initial CV tests with **4a** demonstrated that both couples were reversible at low scan rates (i_{pa}/i_{pc} of 0.95 at 10 mV/s), illustrating stability on CV time scale, electrochemical cycling of **4a** was carried out (see SI for details). The anolyte was dissolved in MeCN, containing 0.5 M TBAPF₆ supporting electrolyte and placed in one side of a divided H-cell. Anolyte **4a** was then reduced, first to **4a**^{•-} and then **4a**^{•2-} by application of a constant current (-5 mA), using a reticulated vitreous carbon (RVC, 100 ppi) electrode. A potential cutoff of -2.3 V was designated, at which point the current was reversed (+5 mA), leading to regeneration of **4a**. To obtain information about stability from this data, this cycle is repeated iteratively. Over the course of 50 cycles (18.3

h), a 17% loss of capacity was observed, corresponding to 1.1% capacity fade/h, with Coulombic efficiency (CE) remaining close to 100% over the course of the experiment. Overall % fade in capacity is defined as the percent of capacity lost relative to the highest overall capacity reached. Initial storage stability tests of **4a** were also carried out via bulk electrolysis, controlling SOC to 80%. CV and NMR showed minimal decomposition after 3 days in storage (see SI for details). Because initial experiments demonstrated that 2,2'-bipyrimidines were capable of undergoing two reversible reductions at low potential, further exploration of these electrolytes was undertaken. To evaluate potential structure-function trends, a subset of substituted 2,2'-bipyrimidines was synthesized, with 24 compounds in total, utilizing the synthetic route described

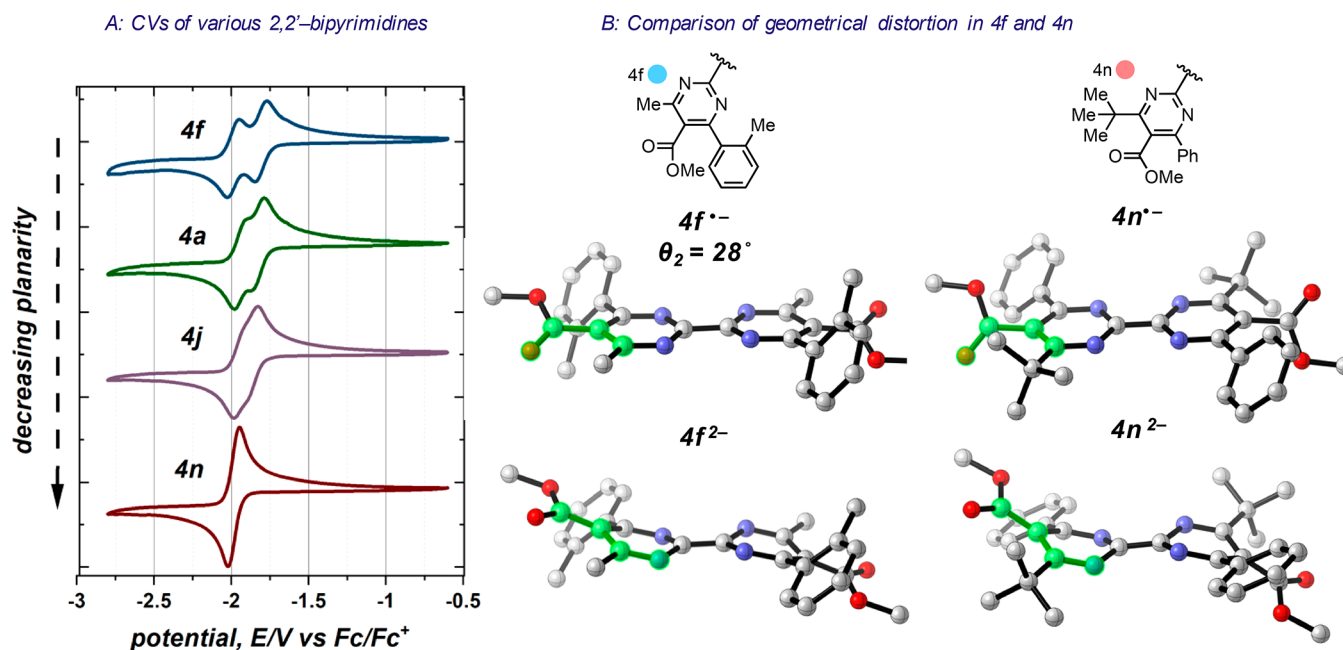


Figure 7. (A) Comparison of cyclic voltammograms of compounds **4f**, **4a**, **4j**, and **4n**, illustrating how structural changes led to differences in relative shifts of $E_{1/2}^1$ and $E_{1/2}^2$. (B) DFT structures of the radical-anion and dianion of compounds **4f** and **4n**, respectively. Greater distortion of the ester group from planarity leads to a cathodic shift in the first redox couple, while distortion of the pyrimidine ring leads to cathodic shift of the second redox couple.

above (Figure 6). With the exception of **4i**, which exhibited poor solubility in MeCN and could not be electrochemically characterized, all molecules synthesized were observed to have reversible couples whose peak currents were linearly dependent on the square-root of scan rate (see SI for details), indicative of a diffusion-controlled electron transfer process. Varying the identity of the ester was found to have subtle effects on redox potentials (compounds **4a–e**), while changes to the substituents on the pyrimidine core led to larger differences. As expected, electron-donating groups generally lead to a negative shift in the redox potential for the two couples, resulting in dialkyl-substituted 2,2'-bipyrimidines (**4r–x**) having more extreme potentials. However, **4q** exhibited the least negative $E_{1/2}$ values for both couples, due to apparent stabilization afforded by the tethered ammonium cation.

Interestingly, the identity of the functionality at the 4 and 6 positions of the bipyrimidine seemed to not only affect $E_{1/2}^1$ and $E_{1/2}^2$ values but also their relative position to each other (Figure 7A). DFT analysis highlighted that due to the steric congestion about the ester functionality at the 5 position, two distinct types of geometrical distortion can occur in the radical-anion ($4^{\bullet-}$) and dianions (4^{2-}) following reduction. As discussed above, the carbonyl group in $4^{\bullet-}$ is distorted from the expected planarity with the aromatic ring. However, in 4^{2-} the pyrimidine ring itself is puckered to achieve resonance delocalization of the anionic charge present at the C5 position, which becomes more impactful in the dianionic charge state (Figure 7B).

Substituents on either side of the ester lead to a systematic effect on the first redox couple, with groups that facilitate a relatively large degree of planarity, leading to less extreme $E_{1/2}^1$ values. For example, **4f** $^{\bullet-}$ bears a 2-tolyl group, which allows a greater degree of planarity of the carbonyl ($\theta_2 = 28^\circ$) due to the orthogonal positioning of the aromatic ring relative to **4a** $^{\bullet-}$. Larger groups, such as the *t*Bu substituent in **4n** $^{\bullet-}$, lead to less

planarization of the carbonyl due to repulsive interactions ($\theta_2 = 61^\circ$) and thus more extreme $E_{1/2}^1$ values. A similar effect is observed when comparing **4f** $^{2-}$ ($\theta_3 = 167^\circ$) and **4n** $^{2-}$ ($\theta_3 = 152^\circ$) where a greater degree of ring puckering is observed when larger substituents are present adjacent to the ester. This distortion effect seems to impact $E_{1/2}^1$ more so than $E_{1/2}^2$, leading to coalescence of the two redox potentials in more hindered 2,2'-bipyrimidines.

H-cell cycling was carried out for each member of the library, illuminating considerable differences in stability based on structural changes, with overall % fade in capacity observed ranging from 15% to 87% and the rate of fade (% fade/h) ranging from 0.71% to 14.0% (Figure 6). Categorization of the electrolytes based on % capacity fade/h during H-cell cycling, which has been shown to be a more reliable metric for analyzing cycling stability than overall capacity fade,^{16,49} illustrated several stability trends in the data (Figure 6, chart).

Empirically, it is evident that bipyrimidines bearing large groups at the 4 and/or 6 positions have a pronounced decrease in stability to electrochemical cycling, as illustrated by compounds **4l–n** as well as **4w** (Figure 6, light red category). A systematic increase in % fade/h is observed when increasing the size of the 4-substituent as seen in the series of compounds, **4a** (Me), **4j** (Et), **4l** (*i*Pr), and **4n** (*t*Bu). Aryl substitution seems to have a generally stabilizing effect, as the majority of the best performing compounds are aryl substituted, although compounds **4o** and **4p**, bearing only methyl groups on the pyrimidine rings, also exhibited comparatively good stability. As observed in previous studies,³⁰ redox potential was not found to be a reliable predictor of stability (Figure 8), although the most stable compounds generally were observed to have less extreme average redox potentials.

Investigation into the Origin of Electrolyte Decomposition. While it was initially surprising that increased steric hindrance increased the rate of decomposition, these general observations led us to consider that geometric distortion of the

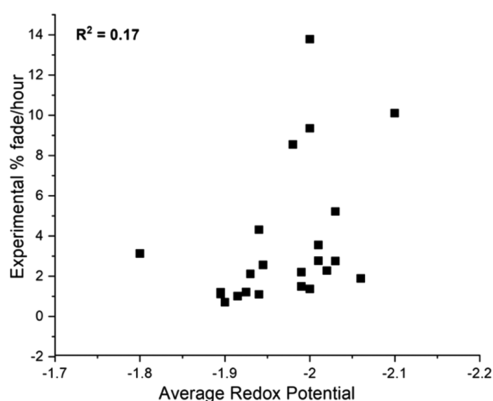


Figure 8. %Fade/h versus the average redox potential for each 2,2'-bipyrimidine.

bipyrimidine could be a contributing factor to decomposition during H-cell cycling. To validate this hypothesis, we endeavored to identify products of decomposition. After each H-cell cycling experiment, a CV was taken to detect any changes (Figure 9).

While several decomposition products were observed throughout the course of the library evaluation, one major distinctive feature was detected in the majority of H-cell cycling experiments (see SI for CVs of all library members). As depicted in Figure 9, when comparing the most and least stable compounds from the initial data set (4f and 4n), an irreversible oxidative feature is observed with an $E_{p/2} \sim -1.0$ V vs Fc/Fc⁺ after 50 charge/discharge cycles. This feature was accompanied by the appearance of a sharp reductive feature with $E_{p/2} \sim -2.7$ V vs Fc/Fc⁺. The appearance of these features correlated with the degree of decomposition of the active electrolyte. Other decomposition products were commonly observed by CV as well, which generally appeared below -2.5 V vs Fc/Fc⁺.

However, independent experiments revealed that these features likely arise from crossover of reactive species from the counter-side of the H-cell and thus are not indicative of the inherent stability of the molecules to electrochemical cycling (see SI for details).

Because a single major decomposition pathway seemed to be responsible for the majority of the observed capacity loss during cycling, further investigation of this decomposition product was undertaken. Due to the rapid decomposition of compound 4n in the respective charge states, this compound was selected as a model to study the relevant decomposition pathway. Bulk electrolysis of a solution of 4n was undertaken at -2.4 V (vs Ag/AgNO₃) to achieve $\sim 100\%$ SOC, subsequently generating the unknown decomposition product, which could be characterized by 2D NMR analysis (Figure 10, see SI for experimental details and characterization). Chemical derivatization of the decomposition product was undertaken by treating the compound with 4-bromobenzyl bromide, allowing for analysis of the resulting products by mass spectrometry. The composition of the resulting compound is consistent with the structure depicted as 6n (Figure 10), and thus, via inference, the decomposition is assigned as 5n, which is formed through protonation of 4n²⁻. To explore how 5n was formed, a separate electrolysis was carried out in d₃-MeCN. Upon ¹H NMR analysis of the resulting reduced material, the diagnostic methine signal was absent while other signals remained unchanged, suggestive of deuteration. Deuterium incorporation was verified via alkylation with 4-bromobenzyl bromide and analysis by mass spectrometry. Taken together, the decomposition pathway is proposed to occur via protonation of the dianion with the solvent.

While other minor decomposition products were present as well, identifying a major pathway of decomposition provided key insight into how more stable electrolytes could be developed. DFT analysis of 5n shows that significant strain is

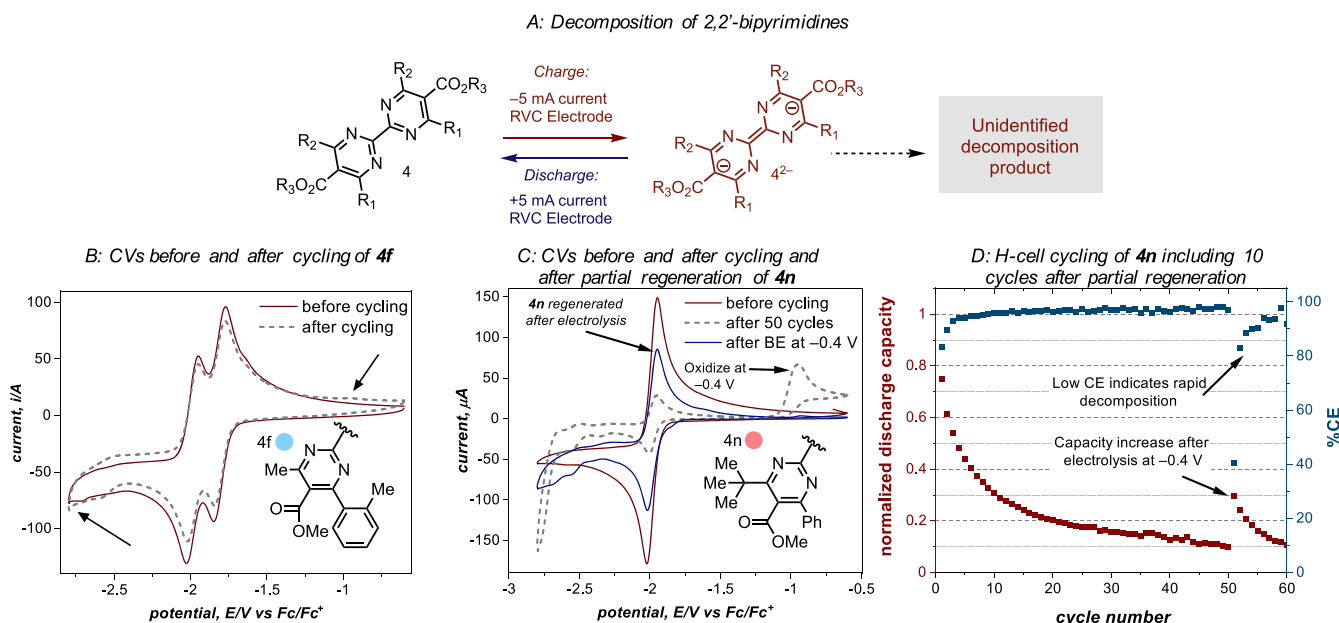
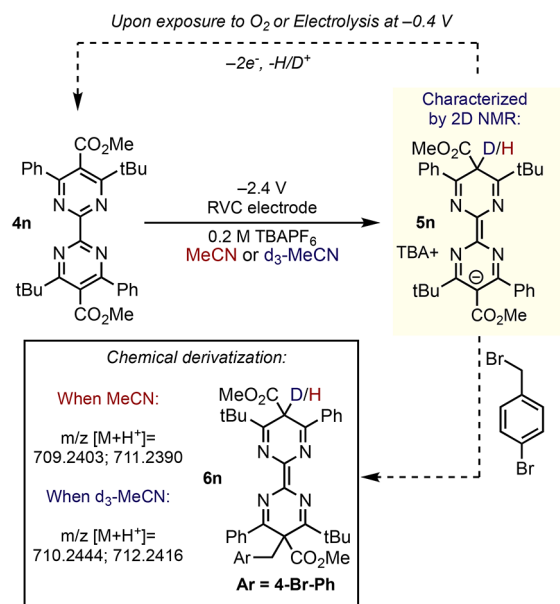


Figure 9. (A) Formation of decomposition product after H-cell cycling experiments (50 cycles). (B) CV before and after H-cell cycling of compound 4f highlighting minimal decomposition. (C) CV after the H-cell cycling of 4n, showing a large degree of decomposition. Bulk electrolysis of the decomposition product at -0.4 V led to the regeneration of 4n. (D) Normalized discharge capacity of 4n vs cycle number. Large decrease in capacity was observed after 50 cycles. After electrolysis of 5n, some capacity was regenerated.

Identification of major decomposition pathway:



DFT computed structure of 5n:

Experimental
 $E_{p/2}^{ox} = -1.03\text{ V}$

Predicted
 $E_{p/2}^{ox} = -0.83\text{ V}$

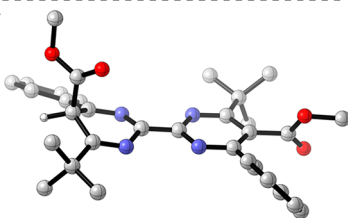


Figure 10. Identification of the major decomposition product via a combination of NMR and chemical derivation analysis.

relieved from 4n²⁻ upon protonation to render the C5 carbon sp³ hybridized and allowing the ester to position itself away from the congested pyrimidine ring. Ring puckering in the remaining reduced pyrimidine ring is also relieved, because the remaining anionic charge can be adequately stabilized via delocalization in the ring system. This is consistent with the hypothesis that geometric strain induced by reduction to the dianionic charge state is primarily responsible for the instability of certain electrolytes.

In considering the decomposition process results from a simple protonation event, a unique avenue for regeneration of redox active material was envisioned, similar to the process of anthraquinone regeneration reported by Aziz and co-workers.²⁸ This was inspired by the observation of 5n (~-1.0 V vs Fc/Fc⁺) undergoing two-electron oxidation upon exposure to ambient air to ultimately regenerate the neutral 2,2'-bipyrimidine 4n via deprotonation as evidenced by ¹H NMR (see SI for details). It was also discovered that 5n could be electrolyzed to partially reform 4n by performing bulk electrolysis at -0.4 V as evidenced by CV (Figure 9C). After 50 electrochemical cycles of 4n, nearly all of the redox active material had been depleted, with only ~10% of the theoretical capacity remaining after 50 cycles. However, upon electrolysis of 5n, a renewal of capacity was observed after 10 additional cycles were carried out, reaching a maximum of ~30% of the theoretical capacity, providing further evidence for the reappearance of 4n (Figure 9D).

Overall, a low Coulombic efficiency (CE) of only 40% was observed for the first cycle following electrolysis, and CE

remained relatively low throughout the remaining nine cycles. This suggests a more rapid decomposition of 4n, and following these 10 cycles, 5n is once again generated. The conversion of 5n back to 4n can be undertaken multiple times. The low CE observed, and rapid conversion back to 5n, is suggestive of buildup of a stronger acid source following the bulk electrolysis. This is likely a consequence of the formation of a cationic intermediate following two-electron oxidation of 5n; however, the acid source has not yet been identified.

To investigate this potential avenue for regeneration of decomposed material further, compound 4l was chemically reduced via potassium naphthalenide in THF, followed by a salt exchange with TBACl in MeCN (Figure 11). After 24 h,

Chemical regeneration of active electrolyte:

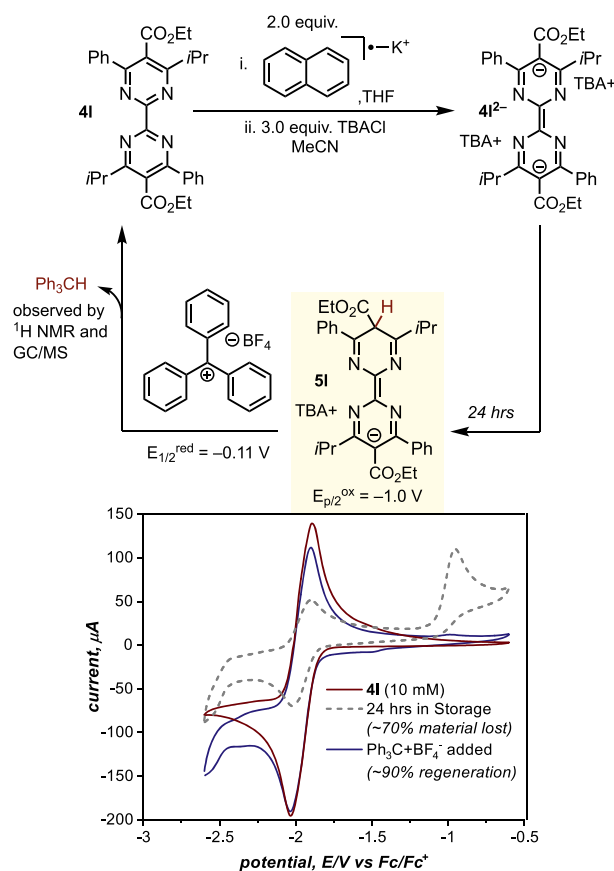
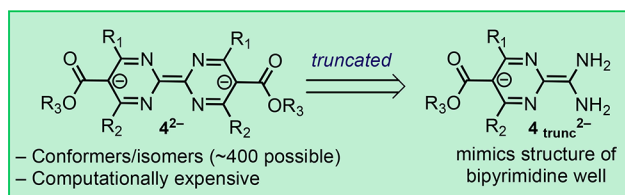


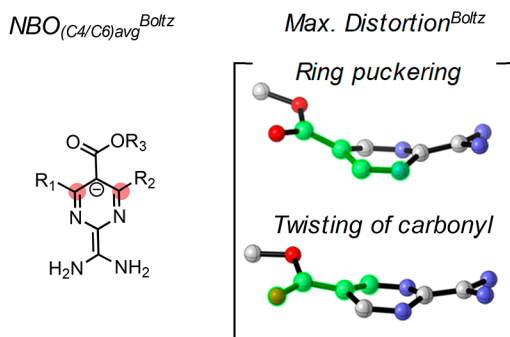
Figure 11. Chemical reduction and decomposition of compound 4l followed by regeneration of the neutral molecule after addition of a hydride scavenger.

significant decomposition to the protonated species was observed by analysis of an aliquot of the solution by CV (~70% of the material was lost based on the CV peak heights). Upon addition of triphenylcarbenium tetrafluoroborate (Ph₃C⁺BF₄⁻) as a formal hydride scavenger, regeneration of 4l was observed by CV (~90% of the decomposed material regenerated) and ¹H NMR, along with the formation of triphenylmethane. It is not clear if the regeneration occurs via a concerted hydride abstraction or via stepwise electron transfer (Ph₃C⁺BF₄⁻, $E_{1/2}^{red} = -0.11\text{ V}$ in MeCN vs Fc/Fc⁺)⁵⁰ followed by H atom abstraction. This method of regenerating bipyrimidines seems to be more efficient than direct

A: Truncation of 2,2'-bipyrimidines for conformational searching



C: DFT parameters



B: Multivariate linear regression modelling

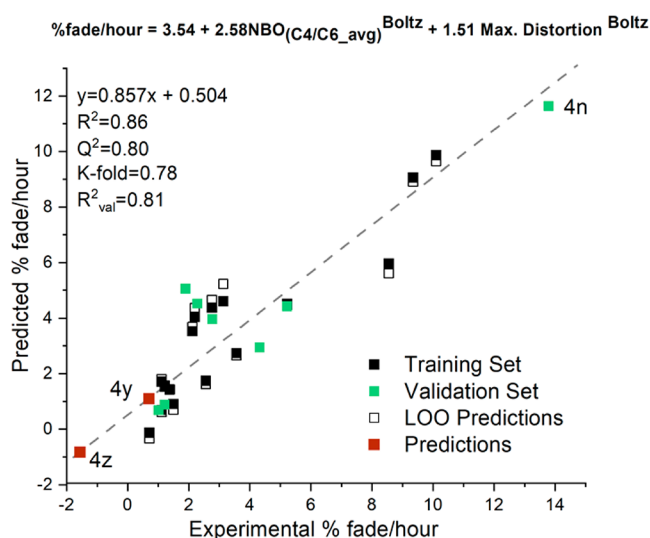


Figure 12. (A) Truncation model for 4^{2-} which drastically decreased the number of conformers that needed to be computed. (B) Multivariate linear regression model relating % capacity fade/h with structural features of the electrolytes. (C) Parameters contained in the model. $NBO_{(C4/C6)avg}^{Boltz}$ is the average, Boltzmann weighted, NBO charge at the C4 and C6 positions on the truncation model. $Max. Distortion^{Boltz}$ is the maximum of the two possible modes of distortion from planarity.

electrolysis, likely because it eliminates acid buildup. With the degradation and regeneration pathways unveiled, future investigations into second-generation bipyrimidine anolytes will be carried out in due course.

Identifying Structure–Activity Trends and Designing Improved Electrolytes. Having identified a decomposition pathway for compound **4n**, we set out to globally test the hypothesis that strain relief plays a significant role in decomposition for the library of compounds evaluated. To probe this, we elected to undertake the development of multivariate linear regression (MLR) models, as it is clear from the empirical data that multiple factors are responsible for the observable changes in decomposition rate. These tools have been commonly used by our lab to relate various experimental outcomes to computationally derived physical properties of chemical compounds.^{51–53} To initiate the analysis, we selected the dianionic species (4^{2-}) to perform feature selection, as this species was experimentally determined to be responsible for the primary decomposition processes (vide supra).

Because conformational flexibility of the substituents at the C4 and C6 positions was likely to have a significant impact on the strain induced in the ring system, we reasoned that conformational analysis was likely to be a key factor in developing effective statistical models.^{54–56} However, conformational searching of the 24 members in the 2,2'-bipyrimidine library revealed that many structures led to an extensive number of conformers and isomers (e.g., conformational searching of $4m^{2-}$ revealed >400 relevant conformers). Therefore, due to the symmetrical nature of the molecules, truncation of 4^{2-} to represent only one-half the molecule (4_{trunc}^{2-}) was undertaken (Figure 12A). This strategy has been used successfully in previous efforts^{57–59} and was found to reduce the number of conformers and isomers drastically.

Using this workflow, conformational searching was performed using the OPLS3 force field⁶⁰ to identify conformers within a 5 kcal/mol energy window of the most stable

conformer. These were subjected to DFT optimization at the M06-2X/6-31+G(d,p) level of theory with CPCM solvation in MeCN. Various features (see SI for details) were then collected from the DFT optimized structures, including Boltzmann weighted parameters. The original 24 library members were split into training (16 electrolytes, black squares) and validation sets (8 electrolytes, green squares) using a pseudorandom automated process.⁵³ MLR analysis was performed using a forward stepwise linear regression algorithm,⁵³ to identify important features that correlate to the experimentally obtained % fade/h data. A statistical model containing two terms was identified (Figure 12B) with an R^2 value of 0.86 indicating a good correlation. Internal ($Q^2 = 0.80$ and $K\text{-fold} = 0.78$) and external ($R^2_{val} = 0.81$) validations were carried out to evaluate the robustness of the model. The two terms found in the model are the average of the NBO charges at the C4 and C6 positions and the maximum distortion from planarity of the truncation model system. Both parameters are derived from Boltzmann weighting of conformers (Figure 12C).

The average NBO charge at the C4 and C6 positions is proposed to generally describe the overall stabilizing effect that aromatic groups have at these positions. The positive coefficient associated with this parameter presumably indicates that electron donating alkyl groups lead to a higher degree of polarization of the C=N double bond. Interestingly, this parameter was found to be the most important descriptor of stability in the model as evidenced by the magnitude of the coefficient, indicating that electron-donating alkyl groups lead to a less stable electrolyte. The distortion from planarity was found to be an important parameter as well, validating our hypothesis that torsional strain built up in the electrolyte upon reduction could lead to more rapid decomposition. Two different modes of distortion were identified during evaluation of the library, underscoring that the identity of the substituents at the C4 and C6 position can change the manner in which 4^{2-}

A: Evaluation of additional 2,2'-bipyrimidines

B: CV before and after cycling 4z

C: Storage stability test of 4z (75% SOC)

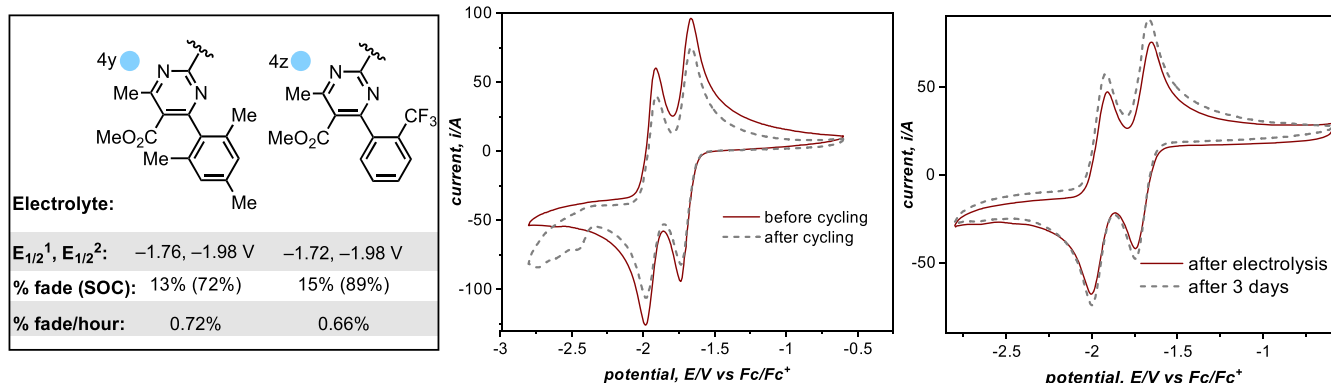


Figure 13. (A) Additional compounds synthesized based on virtual screening. Redox potentials referenced internally vs the Fc/Fc⁺. % Fade = the overall capacity fade observed for each compound. SOC = state of charge. % Fade/h = overall capacity fade/total cycling time. (B) CV before and after electrochemical cycling of 4z highlighting that no decomposition occurring from protonation of the electrolyte was observed. (C) Storage stability test of 4z (40 mM) at 75% SOC (i.e., 50% 4z^{•-} and 50% 4z²⁻). CV of an aliquot was taken after 3 days (~5 mM), highlighting that no visible decomposition was present.

is distorted. As noted previously, large alkyl substituents such as *t*Bu can force puckering of the pyrimidine ring to maintain conjugation with the ester. However, it was also found that interactions between the ester substituent and longer substituents at the C4 and C6 sites can also force the carbonyl out of planarity, even in the dianionic charge state. The most severe of these two modes of distortion was found to correlate to the rate of decomposition.

External validations from the initial data set provided evidence that the model had relatively good predictive capabilities, as demonstrated by the extrapolation of the worst performing electrolyte 4n. We were interested in examining whether this improved understanding of the underlying features of electrolyte stability could be leveraged to design more robust electrolytes. Simultaneously with statistical modeling efforts, virtual screening of several new bipyrimidine structures (focusing on aromatic substituted compounds) revealed that 4y²⁻ and 4z²⁻ should be only modestly distorted from planarity (Figure 13A). Further, after obtaining parameters from the truncated structures, the MLR model predicts that these compounds should be two of the most stable electrolytes (Figure 12B, red squares).

Synthesis of these compounds using the route described above revealed that they experienced low % capacity fade per hour during electrochemical cycling and were indeed two of the most stable compounds, albeit 4y performed equally to the previous best compound 4f. Interestingly, while the prediction for 4y is very close to the experimentally observed value, 4z is predicted by the model to have a negative % fade/h. Due to the physical constraints of the experimental output, linear extrapolation beyond 0% fade/h does not make physical sense but implies that 4z is likely to be a very stable electrolyte. CVs taken of compounds 4y and 4z following H-cell cycling showed no apparent decomposition to the protonated species (Figure 13B, see SI for 4y); however, a decomposition product is apparent at ~-2.5 V vs Fc/Fc⁺. This product was hypothesized to arise from crossover of reactive species from the counter side of the electrochemical cell (see SI for details). We posited that due to some reactivity with reactive counter side material, reading out inherent stability of these molecules

at the limits of the H-cell cycling assay (close to 0.6% fade/h) could be inaccurate.

Storage Stability Tests. To get a more accurate assessment of the inherent stability of the molecules, we conducted storage stability tests for several different classes of compounds, including compounds 4m, 4r, 4y, and 4z. These compounds were selected for storage stability tests to represent a wide range of stability in H-cell cycling but also based on their solubilities in the charged states. Storage stability tests were carried out via bulk electrolysis in a divided cell at four different SOC for each molecule (25%, 50%, 75%, and ~100%). The reduced compounds were then transferred to a separate vessel, and their stability was monitored by acquiring CV over a period of several days. This would allow us to determine the relative stabilities of 4^{•-}, 4²⁻, and mixtures of each. Generally, compounds that were unstable in H-cell cycling were also found to be unstable in storage stability (i.e., 4m and 4r). Unsurprisingly, the rate of decomposition for these compounds increased as the SOC was increased and they were found to be decomposed after 1–2 days in high SOC (see SI for details). Alternatively, compound 4y was found to be relatively stable when only accessing 4y^{•-} (25% and 50% SOC), but gradual decomposition was observed when 4y²⁻ was accessed. Finally, as suggested by MLR models, 4z was found to be stable in high SOC even after 3 days in storage (Figure 13C). Additionally, none of the decomposition products observed during H-cell cycling were formed during the storage stability test, confirming that some degree of decomposition arises from crossover of reactive intermediates during H-cell cycling. This work represents a fundamental investigation into the properties of low potential, two-electron anolytes. These types of anolytes have so far been relatively incompatible with redox flow battery conditions; therefore, a more basic understanding of their properties is necessary to employ anolytes with extreme potentials in a flow battery setting. It is envisioned that further elaboration of the bipyrimidine scaffold could yield a potential anolyte for deployment in a redox flow battery.

CONCLUSIONS

In summary, we have designed a new class of organic anolytes that are capable of storing two electrons at very negative potentials. An initial library of 24 electrolytes was designed and evaluated electrochemically. A large disparity in the stability of these molecules upon electrochemical cycling allowed us to utilize a combination of experimental and computational techniques to identify key structure–function relationships. By characterization of a major decomposition pathway, an avenue for regeneration of the active electrolyte was uncovered, which could have implications for future electrolyte design. Identification of this decomposition product also informed the development of a MLR model that supports the hypothesis of geometrical strain-induced decomposition of 2,2'-bipyrimidines. This allowed us to design an additional anolyte that possessed a higher degree of stability in both electrochemical cycling and multiday storage. Future work in this area will focus on how other properties of these molecules can be improved, particularly solubility.⁶¹ Additionally, continued development of strategies to regenerate decomposed electrolytes in a flow-battery setting is ongoing.

ASSOCIATED CONTENT

Supporting Information

The Supporting Information is available free of charge at <https://pubs.acs.org/doi/10.1021/jacs.0c11267>.

Experimental procedures for all reactions, spectroscopic characterization data for all new compounds, detailed computational methods, copies of ¹H and ¹³C NMR spectra, and Cartesian coordinates (PDF)

AUTHOR INFORMATION

Corresponding Author

Matthew S. Sigman – Department of Chemistry, University of Utah, Salt Lake City, Utah 84112, United States; Joint Center for Energy Storage Research, Argonne, Illinois 60439, United States; orcid.org/0000-0002-5746-8830; Email: sigman@chem.utah.edu

Authors

Jeremy D. Griffin – Department of Chemistry, University of Utah, Salt Lake City, Utah 84112, United States; Joint Center for Energy Storage Research, Argonne, Illinois 60439, United States; orcid.org/0000-0001-9866-8129

Adam R. Pancoast – Department of Chemistry, University of Utah, Salt Lake City, Utah 84112, United States; Joint Center for Energy Storage Research, Argonne, Illinois 60439, United States

Complete contact information is available at: <https://pubs.acs.org/doi/10.1021/jacs.0c11267>

Notes

The authors declare no competing financial interest.

ACKNOWLEDGMENTS

This research was supported by the Joint Center for Energy Storage Research (JCESR), a U.S. Department of Energy, Energy Innovation Hub. J.D.G. thanks the National Institute of Health for financial support through a F32 Ruth L. Kirschstein NRSA fellowship (F32 GM129980). Computational resources were provided from the Center for High Performance Computing (CHPC) at the University of Utah. NMR results

included in this report were recorded at the David M. Grant NMR Center, a University of Utah Core Facility. Funds for construction of the Center and the helium recovery system were obtained from the University of Utah and the National Institutes of Health awards 1C06RR017539-01A1 and 3R01GM063540-17W1, respectively. NMR instruments were purchased with support of the University of Utah and the National Institutes of Health award 1S10OD25241-01. We acknowledge Prof. Shelley Minter for helpful discussions.

REFERENCES

- (1) *World Energy Model*; International Energy Agency: Paris, 2020.
- (2) *Annual Energy Outlook 2020*; U.S. Energy Information Administration, Office of Energy Analysis, U.S. Department of Energy: Washington, DC, 2020.
- (3) Abdmouleh, Z.; Alammari, R. A. M.; Gastli, A. Review of Policies Encouraging Renewable Energy Integration & Best Practices. *Renewable Sustainable Energy Rev.* **2015**, *45*, 249–262.
- (4) Yang, Z.; Zhang, J.; Kintner-Meyer, M. C. W.; Lu, X.; Choi, D.; Lemmon, J. P.; Liu, J. Electrochemical Energy Storage for Green Grid. *Chem. Rev.* **2011**, *111* (5), 3577–3613.
- (5) Johnson, S. C.; Rhodes, J. D.; Webber, M. E. Understanding the Impact of Non-Synchronous Wind and Solar Generation on Grid Stability and Identifying Mitigation Pathways. *Appl. Energy* **2020**, *262*, 114492.
- (6) Liu, W.; Lund, H.; Mathiesen, B. V. Large-Scale Integration of Wind Power into the Existing Chinese Energy System. *Energy* **2011**, *36* (8), 4753–4760.
- (7) Dunn, B.; Kamath, H.; Tarascon, J.-M. Electrical Energy Storage for the Grid: A Battery of Choices. *Science* **2011**, *334* (6058), 928–935.
- (8) Rugolo, J.; Aziz, M. J. Electricity Storage for Intermittent Renewable Sources. *Energy Environ. Sci.* **2012**, *5* (5), 7151.
- (9) Soloveichik, G. L. Flow Batteries: Current Status and Trends. *Chem. Rev.* **2015**, *115* (20), 11533–11558.
- (10) Kear, G.; Shah, A. A.; Walsh, F. C. Development of the All-Vanadium Redox Flow Battery for Energy Storage: A Review of Technological, Financial and Policy Aspects. *Int. J. Energy Res.* **2012**, *36* (11), 1105–1120.
- (11) Luo, J.; Hu, B.; Hu, M.; Zhao, Y.; Liu, T. L. Status and Prospects of Organic Redox Flow Batteries toward Sustainable Energy Storage. *ACS Energy Lett.* **2019**, *4* (9), 2220–2240.
- (12) Viswanathan, V.; Crawford, A.; Stephenson, D.; Kim, S.; Wang, W.; Li, B.; Coffey, G.; Thomsen, E.; Graff, G.; Balducci, P.; Kintner-Meyer, M.; Sprenkle, V. Cost and Performance Model for Redox Flow Batteries. *J. Power Sources* **2014**, *247*, 1040–1051.
- (13) Winsberg, J.; Hagemann, T.; Janoschka, T.; Hager, M. D.; Schubert, U. S. Redox-Flow Batteries: From Metals to Organic Redox-Active Materials. *Angew. Chem., Int. Ed.* **2017**, *56* (3), 686–711.
- (14) Weber, S.; Peters, J. F.; Baumann, M.; Weil, M. Life Cycle Assessment of a Vanadium Redox Flow Battery. *Environ. Sci. Technol.* **2018**, *52* (18), 10864–10873.
- (15) Fernandez-Marchante, C. M.; Millán, M.; Medina-Santos, J. I.; Lobato, J. Environmental and Preliminary Cost Assessments of Redox Flow Batteries for Renewable Energy Storage. *Energy Technol.* **2020**, *8* (11), 1900914.
- (16) Kwabi, D. G.; Ji, Y.; Aziz, M. J. Electrolyte Lifetime in Aqueous Organic Redox Flow Batteries: A Critical Review. *Chem. Rev.* **2020**, *120* (14), 6467–6489.
- (17) Gong, K.; Fang, Q.; Gu, S.; Li, S. F. Y.; Yan, Y. Nonaqueous Redox-Flow Batteries: Organic Solvents, Supporting Electrolytes, and Redox Pairs. *Energy Environ. Sci.* **2015**, *8* (12), 3515–3530.
- (18) Yan, Y.; Robinson, S. G.; Sigman, M. S.; Sanford, M. S. Mechanism-Based Design of a High-Potential Catholyte Enables a 3.2 V All-Organic Nonaqueous Redox Flow Battery. *J. Am. Chem. Soc.* **2019**, *141* (38), 15301–15306.

- (19) Yan, Y.; Vaid, T. P.; Sanford, M. S. Bis(Diisopropylamino)-Cyclopropenium-Arene Cations as High Oxidation Potential and High Stability Catholytes for Non-Aqueous Redox Flow Batteries. *J. Am. Chem. Soc.* **2020**, *142* (41), 17564–17571.
- (20) Cabrera, P. J.; Yang, X.; Suttill, J. A.; Brooner, R. E. M.; Thompson, L. T.; Sanford, M. S. Evaluation of Tris-Bipyridine Chromium Complexes for Flow Battery Applications: Impact of Bipyridine Ligand Structure on Solubility and Electrochemistry. *Inorg. Chem.* **2015**, *54* (21), 10214–10223.
- (21) Sevov, C. S.; Fisher, S. L.; Thompson, L. T.; Sanford, M. S. Mechanism-Based Development of a Low-Potential, Soluble, and Cyclable Multielectron Anolyte for Nonaqueous Redox Flow Batteries. *J. Am. Chem. Soc.* **2016**, *138* (47), 15378–15384.
- (22) Hu, B.; Liu, T. L. Two Electron Utilization of Methyl Viologen Anolyte in Nonaqueous Organic Redox Flow Battery. *J. Energy Chem.* **2018**, *27* (5), 1326–1332.
- (23) Huang, J.; Yang, Z.; Vijayakumar, M.; Duan, W.; Hollas, A.; Pan, B.; Wang, W.; Wei, X.; Zhang, L. A Two-Electron Storage Nonaqueous Organic Redox Flow Battery. *Adv. Sustain. Syst.* **2018**, *2* (3), 1700131.
- (24) Attanayake, N. H.; Kowalski, J. A.; Greco, K. V.; Casselman, M. D.; Milshtein, J. D.; Chapman, S. J.; Parkin, S. R.; Brushett, F. R.; Odom, S. A. Tailoring Two-Electron-Donating Phenothiazines To Enable High-Concentration Redox Electrolytes for Use in Nonaqueous Redox Flow Batteries. *Chem. Mater.* **2019**, *31* (12), 4353–4363.
- (25) Wei, X.; Xu, W.; Huang, J.; Zhang, L.; Walter, E.; Lawrence, C.; Vijayakumar, M.; Henderson, W. A.; Liu, T.; Cosimbescu, L.; Li, B.; Sprenkle, V.; Wang, W. Radical Compatibility with Nonaqueous Electrolytes and Its Impact on an All-Organic Redox Flow Battery. *Angew. Chem., Int. Ed.* **2015**, *54* (30), 8684–8687.
- (26) Wei, X.; Duan, W.; Huang, J.; Zhang, L.; Li, B.; Reed, D.; Xu, W.; Sprenkle, V.; Wang, W. A High-Current, Stable Nonaqueous Organic Redox Flow Battery. *ACS Energy Lett.* **2016**, *1* (4), 705–711.
- (27) Hendriks, K. H.; Sevov, C. S.; Cook, M. E.; Sanford, M. S. Multielectron Cycling of a Low-Potential Anolyte in Alkali Metal Electrolytes for Nonaqueous Redox Flow Batteries. *ACS Energy Lett.* **2017**, *2* (10), 2430–2435.
- (28) Goulet, M.-A.; Tong, L.; Pollack, D. A.; Tabor, D. P.; Odom, S. A.; Aspuru-Guzik, A.; Kwan, E. E.; Gordon, R. G.; Aziz, M. J. Extending the Lifetime of Organic Flow Batteries via Redox State Management. *J. Am. Chem. Soc.* **2019**, *141* (20), 8014–8019.
- (29) Sevov, C. S.; Brooner, R. E. M.; Chénard, E.; Assary, R. S.; Moore, J. S.; Rodríguez-López, J.; Sanford, M. S. Evolutionary Design of Low Molecular Weight Organic Anolyte Materials for Applications in Nonaqueous Redox Flow Batteries. *J. Am. Chem. Soc.* **2015**, *137* (45), 14465–14472.
- (30) Sevov, C. S.; Hickey, D. P.; Cook, M. E.; Robinson, S. G.; Barnett, S.; Minter, S. D.; Sigman, M. S.; Sanford, M. S. Physical Organic Approach to Persistent, Cyclable, Low-Potential Electrolytes for Flow Battery Applications. *J. Am. Chem. Soc.* **2017**, *139* (8), 2924–2927.
- (31) Kober, E. M.; Sullivan, B. P.; Meyer, T. J. Solvent Dependence of Metal-to-Ligand Charge-Transfer Transitions. Evidence for Initial Electron Localization in MLCT Excited States of 2,2'-Bipyridine Complexes of Ruthenium(II) and Osmium(II). *Inorg. Chem.* **1984**, *23* (14), 2098–2104.
- (32) Lumpkin, R. S.; Kober, E. M.; Worl, L. A.; Murtaza, Z.; Meyer, T. J. Metal-to-Ligand Charge-Transfer (MLCT) Photochemistry: Experimental Evidence for the Participation of a Higher Lying MLCT State in Polypyridyl Complexes of Ruthenium(II) and Osmium(II). *J. Phys. Chem.* **1990**, *94* (1), 239–243.
- (33) England, J.; Scarborough, C. C.; Weyhermüller, T.; Sproules, S.; Wieghardt, K. Electronic Structures of the Electron Transfer Series $[M(\text{Bpy})_3]_n$, $[M(\text{Tpy})_2]_n$, and $[\text{Fe}(\text{Tbpy})_3]_n$ ($M = \text{Fe}, \text{Ru}; n = 3+, 2+, 1+, 0, 1-$): A Mössbauer Spectroscopic and DFT Study. *Eur. J. Inorg. Chem.* **2012**, *2012* (29), 4605–4621.
- (34) Sathyamoorthi, S.; Kanagaraj, M.; Kathiresan, M.; Suryanarayanan, V.; Velayutham, D. Ethyl Viologen Dibromide as a Novel Dual Redox Shuttle for Supercapacitors. *J. Mater. Chem. A* **2016**, *4* (12), 4562–4569.
- (35) DeBruiler, C.; Hu, B.; Moss, J.; Liu, X.; Luo, J.; Sun, Y.; Liu, T. L. Designer Two-Electron Storage Viologen Anolyte Materials for Neutral Aqueous Organic Redox Flow Batteries. *Chem.* **2017**, *3* (6), 961–978.
- (36) Liu, W.; Liu, Y.; Zhang, H.; Xie, C.; Shi, L.; Zhou, Y.-G.; Li, X. A Highly Stable Neutral Viologen/Bromine Aqueous Flow Battery with High Energy and Power Density. *Chem. Commun.* **2019**, *55* (33), 4801–4804.
- (37) Yamamoto, K.; Chen, Y. G.; Buono, F. G. Oxidative Dehydrogenation of Dihydropyrimidinones and Dihydropyrimidines. *Org. Lett.* **2005**, *7* (21), 4673–4676.
- (38) Lu, J.; Ma, H. Iron(III)-Catalyzed Synthesis of Dihydropyrimidinones. Improved Conditions for the Biginelli Reaction. *Synlett* **2000**, *2000* (01), 63–64.
- (39) Zhou, Y.; Lin, C.; Xing, Y.; Chen, L.; Yan, X. Efficient Construction of the Nucleus of Rosuvastatin Calcium. *J. Heterocycl. Chem.* **2017**, *54* (3), 1898–1903.
- (40) Sugimoto, O.; Mori, M.; Tanji, K. A Facile Halogenation of Some Hydroxyheterocycles Using Triphenylphosphine and N-Halosuccinimide. *Tetrahedron Lett.* **1999**, *40* (42), 7477–7478.
- (41) Sugimoto, O.; Mori, M.; Moriya, K.; Tanji, K. Application of Phosphonium Salts to the Reactions of Various Kinds of Amides. *Helv. Chim. Acta* **2001**, *84* (5), 1112–1118.
- (42) Buonomo, J. A.; Everson, D. A.; Weix, D. J. Substituted 2,2'-Bipyridines by Nickel Catalysis: 4,4'-Di-Tert-Butyl-2,2'-Bipyridine. *Synthesis* **2013**, *45* (22), 3099–3102.
- (43) It should be noted that efforts to expand the scope of the electrochemical homocoupling beyond **3a** gave yields comparable to that of the traditional method; this could be a reflection of anolyte instability in the charged state because, under the reaction conditions, the bipyrimidine product is likely reduced.
- (44) Zhao, Y.; Yu, Z.; Robertson, L. A.; Zhang, J.; Shi, Z.; Bheemireddy, S. R.; Shkrob, I. A.; Y Z; Li, T.; Zhang, Z.; Cheng, L.; Zhang, L. Unexpected Electrochemical Behavior of an Anolyte Redoxmer in Flow Battery Electrolytes: Solvating Cations Help to Fight against the Thermodynamic–Kinetic Dilemma. *J. Mater. Chem. A* **2020**, *8* (27), 13470–13479.
- (45) Zhao, Y.; Truhlar, D. G. The M06 Suite of Density Functionals for Main Group Thermochemistry, Thermochemical Kinetics, Noncovalent Interactions, Excited States, and Transition Elements: Two New Functionals and Systematic Testing of Four M06-Class Functionals and 12 Other Functionals. *Theor. Chem. Acc.* **2008**, *120* (1), 215–241.
- (46) Barone, V.; Cossi, M. Quantum Calculation of Molecular Energies and Energy Gradients in Solution by a Conductor Solvent Model. *J. Phys. Chem. A* **1998**, *102* (11), 1995–2001.
- (47) Cossi, M.; Rega, N.; Scalmani, G.; Barone, V. Energies, Structures, and Electronic Properties of Molecules in Solution with the C-PCM Solvation Model. *J. Comput. Chem.* **2003**, *24* (6), 669–681.
- (48) DFT calculations were performed without inclusion of counter-cations, which is likely to affect the absolute magnitude of rotational barriers.
- (49) Kowalski, J. A.; Neyhouse, B. J.; Brushett, F. R. The Impact of Bulk Electrolysis Cycling Conditions on the Perceived Stability of Redox Active Materials. *Electrochem. Commun.* **2020**, *111*, 106625.
- (50) Connelly, N. G.; Geiger, W. E. Chemical Redox Agents for Organometallic Chemistry. *Chem. Rev.* **1996**, *96* (2), 877–910.
- (51) Sigman, M. S.; Harper, K. C.; Bess, E. N.; Milo, A. The Development of Multidimensional Analysis Tools for Asymmetric Catalysis and Beyond. *Acc. Chem. Res.* **2016**, *49* (6), 1292–1301.
- (52) Guo, J.-Y.; Minko, Y.; Santiago, C. B.; Sigman, M. S. Developing Comprehensive Computational Parameter Sets To Describe the Performance of Pyridine-Oxazoline and Related Ligands. *ACS Catal.* **2017**, *7* (6), 4144–4151.

(53) Santiago, C. B.; Guo, J.-Y.; Sigman, M. S. Predictive and Mechanistic Multivariate Linear Regression Models for Reaction Development. *Chem. Sci.* **2018**, *9* (9), 2398–2412.

(54) Robinson, S. G.; Yan, Y.; Hendriks, K. H.; Sanford, M. S.; Sigman, M. S. Developing a Predictive Solubility Model for Monomeric and Oligomeric Cyclopropenium-Based Flow Battery Catholytes. *J. Am. Chem. Soc.* **2019**, *141* (26), 10171–10176.

(55) Miró, J.; Gensch, T.; Ellwart, M.; Han, S.-J.; Lin, H.-H.; Sigman, M. S.; Toste, F. D. Enantioselective Allenolate-Claisen Rearrangement Using Chiral Phosphate Catalysts. *J. Am. Chem. Soc.* **2020**, *142* (13), 6390–6399.

(56) Werth, J.; Sigman, M. S. Connecting and Analyzing Enantioselective Bifunctional Hydrogen Bond Donor Catalysis Using Data Science Tools. *J. Am. Chem. Soc.* **2020**, *142* (38), 16382–16391.

(57) Yamamoto, E.; Hilton, M. J.; Orlandi, M.; Saini, V.; Toste, F. D.; Sigman, M. S. Development and Analysis of a Pd(0)-Catalyzed Enantioselective 1,1-Diarylation of Acrylates Enabled by Chiral Anion Phase Transfer. *J. Am. Chem. Soc.* **2016**, *138* (49), 15877–15880.

(58) Crawford, J. M.; Stone, E. A.; Metrano, A. J.; Miller, S. J.; Sigman, M. S. Parameterization and Analysis of Peptide-Based Catalysts for the Atroposelective Bromination of 3-Arylquinazolin-4(3H)-ones. *J. Am. Chem. Soc.* **2018**, *140* (3), 868–871.

(59) Crawford, J. M.; Sigman, M. S. Conformational Dynamics in Asymmetric Catalysis: Is Catalyst Flexibility a Design Element? *Synthesis* **2019**, *51* (5), 1021–1036.

(60) Harder, E.; Damm, W.; Maple, J.; Wu, C.; Reboul, M.; Xiang, J. Y.; Wang, L.; Lupyan, D.; Dahlgren, M. K.; Knight, J. L.; Kaus, J. W.; Cerutti, D. S.; Krilov, G.; Jorgensen, W. L.; Abel, R.; Friesner, R. A. OPLS3: A Force Field Providing Broad Coverage of Drug-like Small Molecules and Proteins. *J. Chem. Theory Comput.* **2016**, *12* (1), 281–296.

(61) Preliminary efforts to measure solubility show that compound **4z** has only a moderate solubility in MeCN (0.1 M), while the dianionic charge state (**4z**²⁻) seems to be a miscible oil when TBA⁺ counterions are utilized.